IIETA International Information and Engineering Technology Association
Advancing the World of Information and Engineering

Journal of New Materials for Electrochemical Systems
Vol. 27, No. 3, September 2024, pp. 215- 226
Journal homepage: http://iieta.org/journals/jnmes

Optimizing Supercapacitor Performance with LSCF, ST, BST, and Coconut Shell Activated Carbon

J.Lurdhumary[1],P. Hosanna Princye[2], Arul Prakash M[3], L.Sangeetha[4], G.S.V. Seshu Kumar[5], S. Maheswari[6], Kirubakaran D[7], L. Umaralikhan[8] and V. Vijayan[9]

[1] Department of Electronics and Communication Engineering, Sri Sai Ram Institute of Technology, Chennai, Tamil Nadu 600044, India
[2] Department of Electronics and Communication Engineering, Sri Sairam College of Engineering, Bangalore, Karnataka 562106, India
[3] Department of Mechanical Engineering, Sri Sai Ram Engineering College, Chennai, Tamil Nadu 600044, India.
[4] Department of Physics, Saveetha Engineering College, Thandalam, Chennai, Tamil Nadu 602105, India.
[5] Department of Mechanical Engineering, SRKR Engineering College, Bhimavaram, Andhra Pradesh 534204, India.
[6] Department of Electrical and Electronics Engineering, Kongu Engineering College, Perundurai, Tamil Nadu 638060, India.
[7] Department of Electrical and Electronics Engineering, St. Joseph's Institute of Technology, Chennai, Tamil Nadu 600119, India
[8] Department of Physics, Jamal Mohamed College (Autonomous), Trichy, Tamil Nadu 620020, India
[9]Department Mechanical Engineering, K. Ramakrishnan College of Technology, Tiruchirappalli 621112, India

Corresponding Author Email: *vijayan.me@gmail.com*

https://doi.org/10.14447/jnmes.v27i3.a07

Received: 18/01/2024
Accepted: 08/08/2024

Keywords:
Spray pyrolysis, Activated carbon, Perovskite materials, Ferroelectrics, Supercapacitor Energy storage.

ABSTRACT

Emerging electrochemical devices including fuel cells, supercapacitors, and lithium-ion batteries are crucial for energy conservation, storage, and transfer. When looking for a replacement for traditional batteries, electrochemical supercapacitors offer a viable option due to their long cycling life and high power supply capabilities. Problems with their high production cost and poor energy density, however, prevent their widespread use. Presenting here is the novel merging of perovskite (LSCF, BST, ST) and CSAC (coconut shell-based activated carbon) materials produced in a thin layer by spray pyrolysis. The integration of the electroactive medium with the double-layer electrode in electrochemical supercapacitors expands upon earlier research. Using cyclic voltammetry, electrochemical impedance spectroscopy, galvanostatic charge/discharge profiling, and modeling of the experimental data, the performance and dynamic electrical behavior of different supercapacitor topologies were examined for utilization in power applications. These structures, which were made of cotton lint and organic cellulose were shaped like asymmetric coin cells. Mixing BST with cellulose results in supercapacitors with 300 F/g specific capacitances, energy densities of 6.7 Wh/kg, power densities of 600 W/kg, and the ability to preserve over 95% of their initial capacitance even after multiple charging and discharging cycles. Based on these promising features, we demonstrated the practicality of our supercapacitor approach by connecting two identical cells and briefly powering a yellow LED. This breakthrough will pave the way for the development of supercapacitors that are more pliable, lightweight, and affordable, and which may have better energy-storing capabilities and longer lifespans.

1. INTRODUCTION

In today's society, finding new energy sources is absolutely critical. The need can be satisfied by the creation of novel energy storage devices. Nevertheless, attaining great efficiency is not without its difficulties. More effective energy storage systems are the goal of the current, never-ending quest for novel, multipurpose materials [1], [2]. An increasing number of important new technologies for energy storage, transport, and conservation are electrochemical devices. Some examples of these are supercapacitors, fuel cells, and lithium-ion batteries. Despite the continuous improvement in both cost and performance of these devices, optimizing the materials that comprise them remains a significant problem. Electrochemical supercapacitors were the alternatives to traditional energy storage devices can supply both long cycling life and high power. Nevertheless, their potential for advancement is hindered

by their high production costs and low energy density. In an endeavor to greatly enhance the specific capacitance of these devices, numerous research groups worldwide are developing new materials for the electrodes, separators, electrolytes, and dielectric media of supercapacitors. Many perovskites with trivalent, divalent, or tetravalent cations find use as electrodes, electroactive dielectrics, or solid-state electrolytes for supercapacitors. Energy storage systems find several uses for these materials. An electrical condenser, a supercapacitor makes use of the characteristics of charge distribution at electrode-electrolyte interface. A better understanding of how charge energy is stored and the creation of advanced nanostructured materials have both contributed to supercapacitors performing better [3].

Electrochemical conversion allows supercapacitors to hold charge, making them a safe and clean energy source. Other benefits of supercapacitors include longer cycle life, faster charge and discharge times, better power densities, and more [4], [5]. While electrostatic interactions are utilized by both pseudocapacitors and electrochemical double-layer capacitors (EDLCs), the latter rely on the redox reactions of electrode materials for energy storage. A hybrid supercapacitor, which combines electrolyte drop capacitors (EDLCs) with basic pseudocapacitors, can store more energy and have a larger capacitance than either the standard EDLC or the simple pseudocapacitor [6]. The power density of hybrid supercapacitors is higher than that of fuel cells and batteries, but their energy density is lower [7]. In contrast, hybrid supercapacitors have the potential to provide a specific capacitance that is far greater than that of traditional capacitors [8]. The energy storage capacity and maximum instantaneous power output of a supercapacitor are directly related to its capacitance. Capacitance is the ratio of stored charge at equivalent series resistance, Rs and interface to applied voltage as shown in Equations (1) and (2)[9], [10].

$$E = \frac{1}{2}CV^2 \quad (1)$$

$$P_{\max} = \frac{V^2}{4R_S} \quad (2)$$

Improvements in total capacitance and cell voltage are necessary for hybrid supercapacitors to solve the problem of poor energy density. To meet these demands for better knowledge of ion transport mechanisms and the development of novel materials, there are a number of intense and sophisticated approaches. To enhance capacitance, combine electrode materials such as metal oxides with electrochemically active materials like activated carbon, which possess a high surface area and porous structure [11], [12]. Another option is to add redox additives to traditional electrolytes, which will increase the pseudocapacitance contribution between the electrode and electrolyte. An increase in cell voltage is possible by the use of electroactive materials' redox processes, EDLC, and asymmetric electrodes. Since the maximum cell voltage is usually restricted by dielectric breakdown strength, and maximum energy storage was obtained. Further considerations including electrolyte's stability, dielectric thickness, effective surface area of electrodes, and resistance of the capacitor's internal components. Although it has not been simple to simultaneously avoid all of these drawbacks, hybrid supercapacitors founded on novel materials have demonstrated that they can improve energy and capacitance by a factor of roughly 10,000 compared to ordinary capacitors. In order to produce these materials at low temperatures during phase synthesis, scientists worldwide are presently using a wide variety of processes, including co-precipitation, nano casting, sol-gel, hydrothermal, combustion, spray pyrolysis, thermal decomposition, and many more. Among these methods, spray pyrolysis (SP) stands out as a versatile technique that has become increasingly popular for making thick and thin films that incorporate electroactive materials and electrodes for application in supercapacitors [13]. Sp is a continuous deposition process that is fast, simple, and applicable to aerosol activities.

Parameters such as precursor concentration, substrate temperature, and spray solution rate can be adjusted to alter the film's stoichiometry and shape. Due to its low running cost and potential for deposition in wide areas, SP has a very promising future in industrial applications [14], [15]. Our research and development of electrochemical supercapacitors using perovskite materials as a hybrid for both electrochemical and electrostatic charge storage is detailed here. There have been earlier descriptions of many perovskite materials that exhibit remarkable dielectric, ferromagnetic, ferroelectric, and multiferroic properties. Gas sensors, photovoltaic cells, optoelectronics, energy storage devices, non-volatile ferroelectric random-access memory, high dielectric capacitors and these materials are used in a variety of associated industries. In this study, we created a perovskite transition metal oxide called La0.85Sr0.15MnO3 (LSCF).

The low resistance and high specific capacitance of this material make it an ideal electrode material. Additionally, we used high dielectrics/ferroelectrics perovskites as PbZr0.52Ti0.48O3 (ST) and $BaTiO_3$ (BST) as electroactive media to construct inexpensive coin cell supercapacitor (CCS) devices[16], [17]. The electrical, electrochemical, structural, and porous properties of these materials were studied prior to making and testing the CCS devices. A flexible and heterogeneous layered structure of electrodes and dielectrics was designed using the spray pyrolysis process on Al and Cu substrates. An aqueous solution was utilized to soak cellulose and cotton fabric lint, which served as separator layers to finish the CCS devices. Additionally, we compared the tested CCSS devices' performance. The findings of this study may pave the way for the creation of supercapacitors using stable anion-intercalation-type perovskite materials, which are known for their outstanding performance.

2. EXPERIMENTAL METHODOLOGY

2.1. Fabrication of (La0.6Sr0.4Co0.2Fe0.8O3-δ, LSCF)

Lanthanum Strontium Cobalt Ferrite (LSCF) perovskite (La0.6Sr0.4Co0.2Fe0.8O3-ά, LSCF) was synthesized using a solid-state method similar to previous powder perovskites made of metal oxides [18], [19], [20]. The procedure required the correct proportions of La, Sr, Co, Fe, and O, high purity raw ingredients (~99%), to be mixed in isopropyl alcohol. The powder that was produced was heated at 1000ºC for six hours

and reheated at 1200ºC for four hours in order to achieve a single-phase perovskite structure and good powder crystallization.

2.2. Fabrication of $SrTiO_3$

Strontium Titanate ($SrTiO_3$) was synthesized by the conventional solid-state technique. The raw ingredients, with a purity level of 99% for SrO and 99% for TiO_2, were mixed together in isopropyl alcohol as milling using suitable SrO: TiO_2 ratio. They were in powder oxide form. The stoichiometric composition was adjusted to include an excess of 10 mol% SrO in order to achieve higher densification and prevent lead deficiency during synthesis. The agglomerates were released by grinding the dried material with the mortar. To get a solid perovskite structure with enough crystallization, the powder is then calcined at 850 °C for 6 hours and re-heated at 900°C for 4 hours.

2.3. Preparation of ($Ba1\text{-}xSrxTiO_3$, BST)

A stoichiometric mixture of high-purity barium carbonate ($CSACO_3$), titanium dioxide (TiO_2) and strontium carbonate ($SrCO_3$) proved the best precursor for synthesizing barium strontium titanate ($Ba1\text{-}xSrxTiO_3$, where x is the strontium component). The two precursors were dissolved in glacial acetic acid and swirled magnetically at 60 ºC for 1 hour. To achieve a consistent and see-through gel, ethylene-glycol was gradually added. After being dried thoroughly, the gel was filtered to make a stock solution. Subsequently, the clumps were ground by hand into a fine powder. A single-phase perovskite structure and good powder crystallization were achieved by subjecting the powder to calcination at 400°C for 4 hours to remove organic residues, followed by heating it to 950°C for 5 hours, and finally to 1000°C for re-heating.

2.4. Formation of activated carbon

The coconut shells were pulverized and sieved into a fine sawdust, which was then used to make activated carbon. The timber was converted into coconut shell charcoal (CSC) through thermochemical decomposition through pyrolysis in a nitrogen environment at 650◦C. The CSC was subsequently chemically activated with H_3PO_4. Then, in a nitrogen environment, the CSC was heated to temperatures ranging from ambient temperature to 750◦C. Using distilled water, the coconut shell-activated carbon (CSAC) that was produced was rinsed until its pH reached neutral. At last, the CSAC was reduced to a fine powder by drying, grinding, and sieving it.

2.5. Structural analysis

The structural properties of carbonaceous and perovskites materials were examined using a Rigaku SmartLab X-ray diffractometer that is equipped with Cu-K α(λ = 1.5046 ô) radiation. Through the comparison of experimental patterns with structures in the ICDD and ICSD databases, the phase composition of the perovskite was determined.

2.6. Electrical analysis of electrodes

The electrical efficiency of LSCF and LSCF+CSAC beads was evaluated using room temperature ac impedance spectroscopy on an automated 3522/3532-50 LCR HiTester. Using silver paint to metalize the pellets on both sides allowed for the achievement of the 1.23 cm^2 two-electrode capacitor design. The experiment was run with a 10 mV ac voltage and frequencies between 1 Hz and 1 MHz.

2.7. Electrochemical analysis of electrodes

Producing LSCF and a 4:1 LSCF + CSAC powder was the initial stage in performing electrode testing. Two milligrams of each powder were manually added and mixed into 1 ml of a mixture containing isopropanol, ethanol, nafion, and water at a ratio of 2:1:1:0.1. Subsequently, a carbon electrode with polished surface and 0.08 cm^2 geometric area was covered with 5 µL of both the LSCF and LSCF + CSAC inks. The three-electrode arrangements were made using the glass cell. We utilized the aforementioned materials for the working electrodes and Silver/Silver Chloride for the reference electrode. Plating wire served as the counter electrode. An electrolyte solution containing 1 M KOH was subsequently added to the cell. We used galvanostatic charge/discharge (GCD) profiles at constant current by a potentiostat station and cyclic voltammetry (CV) curves with scan speeds ranging from 10 to 100 mV/s to assess the electrochemical behaviour of LSCF and LSCF+CSAC electrodes.

2.8. Ferro-electrical analysis of St and BST

At ambient temperature, the RT6000HVS, a ferroelectric workstation, was used to measure the hysteresis loops (polarization) vs. (electric field) of ferroelectrics BST and ST in unipolar mode.

2.9. Spray pyrolysis

In the electrochemical supercapacitor fabrication methodology, the films were systematically deposited using the spray pyrolysis (SP) method. Spray pyrolysis, depicted in Figure 1 is a common method for producing dielectric films, electrodes, and substrates. An isopropyl alcohol solution was made by dissolving 1 gram of polyvinylpyrrolidone in 10 ml of water using magnetic stirrer at 60ºC. After that, a 4:1 molar ratio of CSAC and 1 g of LSCF powder were added to the polymeric solution. After a magnetic stirring for an hour at room temperature, the liquid was sonified to produce an ink that was homogeneous enough for electrode formation. Mixing 2 grams of ferroelectric powder (ST or BST) with 10 ml of polymeric solution and swirling it magnetically for 1 hour at room temperature yielded a homogeneous ink that could be used to create electroactive medium.

The airbrush was used to apply the electrode ink. Carefully placed on a hot plate at 80ºC, high-purity copper sheets and aluminum measuring 95 × 95 × 40 mm served as substrate. A spray nozzle with a diameter of 0.38 mm was placed 15 cm away from the substrates so that the aerosol particles could reach them as a fine mist. Afterwards, 5 ml of ink was applied to every substrate using an airbrush operating at a pressure of 40 Psi with 0.8 ml/min steady flow rate. After the deposition process is complete, the substrates are given a full day to dry. To coat the electrode layer, we did it again, this time using an airbrush

loaded with dielectric ink. Finally, on the metal substrates, we obtained flexible films that were approximately 200 mm thick.

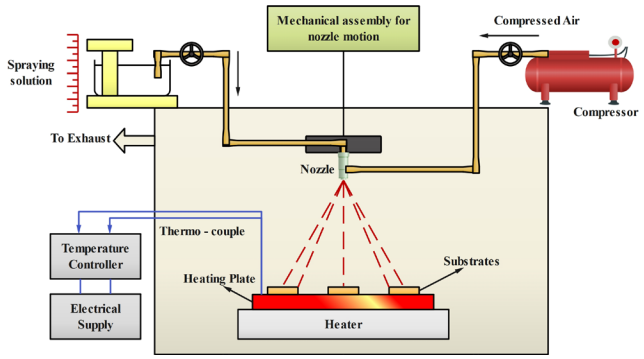

Figure 1. Fabrication of metal/electrode/dielectric layers for electrochemical SCs, spray pyrolysis is utilized.

2.10. Construction and design of coin cell supercapacitor (CCS) apparatus

We constructed four supercapacitors with varying designs to analyze and improve their performance. Here are the specifics of the completed set. Circular sheets with 10 mm diameters and 0.8 cm^2 surface areas were cut from the LSCF+CSAC/dielectric films coated with copper and Aluminium substrates using a metal hole puncher. Copper isutilized as cathode and aluminium as anode in the two-electrode designs according to their reduction potential. A loading mass of approximately 20 mg was observed in the LSCF+CSAC/dielectric heterostructure film. A synthetic polymer gel solution was used as the electrolyte. This was made by mixing 0.2 g of polyvinylpyrrolidone (PVP) powder with 10 ml of isopropyl alcohol and 0.5 ml of H_3PO_4in 30 ml of distilled water. Separator layers were formed of cotton lint fabric and self-made cellulose membranes, with dimensions of 15 mm in diameter, approximately 200 mm in thickness, and approximately 27 mg in mass. Before being sandwiched between electrodes, each layer of the separator is thoroughly wetted in electrolyte.

2.11. Characterization by electrochemical means of CCS devices

In order to conduct the electrochemical characterization of CCS devices, BioLogic instruments utilized the SP-200 potentiostat. The three techniques utilized for characterization include cyclic voltammetry (CV), electrochemical impedance spectroscopy (EIS) with a two-electrode configuration, and galvanostatic charge-discharge (GCD). The frequency range that the EIS analysis was conducted inside was from 1 MHz to 0.01 mHz. Potentially usable scan speeds for CV analysis were 10–120 mV/s, and the voltage window was 0-0.4 V. Fifty charge/discharge cycles were conducted for the GCD investigation with a voltage ranging from 0-0.4 V and a current rate of 100 mV/s.

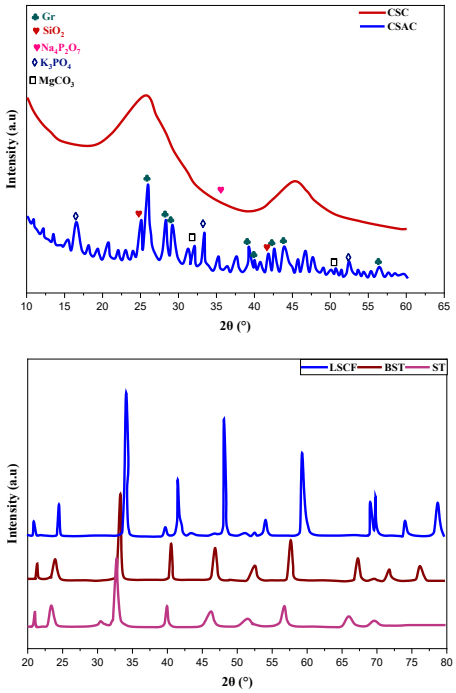

Figure 2. XRD pattern of (a) CSC and CSAC and (b) LSCF, BST, ST samples.

3. RESULTS AND DISCUSSION

3.1. Perovskite and carbonaceous material structural analysis

Figure 3 displays the X-ray diffraction (XRD) phase structure of carbonaceous CSC and CSAC powders. The LSCF, BST, and ST processes revealed remarkably pure phases, leading to formation of perovskite structures. In agreement with conventional XRD ICDD cards, our findings provide XRD patterns and crystal structure. According to the database entries, the LSCF structure is classified as orthorhombic phase with lattice dimensions. Meanwhile, BST is identified as a tetragonal phase with lattice parameters.

When the peak appears at approximately 24º, it means that the crystalline structure is becoming more regular, which means that the layers are more aligned. The CSC structure can be compared to the hexagonal structure according to the ICDD card #7740-44-0 [21], [22]. Both CSC peaks vanished throughout the H_3PO_4 activation phase, and numerous lattice defects formed, perhaps as a result of P intercalation and C evaporation. Theweak reflections on CSAC structure are likely formed carbonates and phosphates, as the CSAC EDX spectrum shows only trace levels of Mg, P, Na, S, Si, and K. Inset Fig. 2 right shows the XRD pattern that was used to identify and mark these impurity phases.

3.2. Elemental composition

The samples were examined for their chemical and elemental composition through EDX. Figure 3 displays the chemical and elemental composition ofLSCF, ST, BST, and CSAC. Every single perovskite and carbonaceous substance has its components and chemical compositions verified by EDX tests.

In contrast, CSAC's chemical composites includes agglomerates of trace elements like K, P, Si, Na, Mg, and S on its porous surface. An aggregate of approximately 1.3 µm is depicted in the inset on the right side of figure 3. The phosphoric acid that was utilized for the activation is the principal source of the P that is present [23], [24]. In order to remove any ions, salt, or residual chemicals, the CSAC was rinsed extensively after activation. Secondary phases can be created by subjecting the material to high temperatures during thermal treatment. These findings provide credence to the activated carbon diffraction pattern, which reveals the sparse deposition of these supporting components onto the porous carbon surface. The graphite crystalline structure on the carbon surface had been partially changed. The introduction of amorphous carbon into the structure took place as a result of the breaking of the (002) and (101) phases during the formation of a porous structure using smaller fragments.

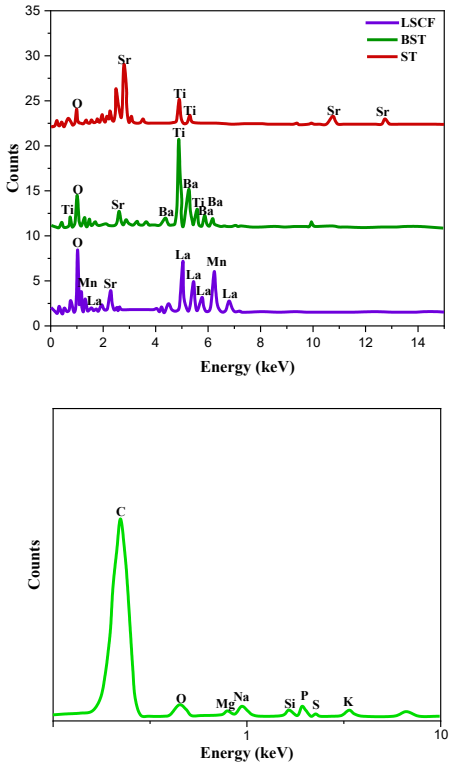

Figure 3. Elemental composition and EDX analysis of LSCF, BST, ST, and CSAC samples.

3.3. Carbonaceous substance surface analysis

The specific surface area and pore size of CSC and CSAC were better understood through nitrogen adsorption-desorption experiments performed at atmospheric temperature. At high relative pressure, these carbonaceous materials do not impede adsorption, and their slit-shaped pores are characteristic of microporous adsorbents. They follow what is known as a Type II isotherm in gas adsorption-desorption, as defined by the IUPAC. In 0.4 to 0.5 relative pressure range, CSAC has a sharper desorption curve slope than CSC, as can be seen from the comparison of the two curves.

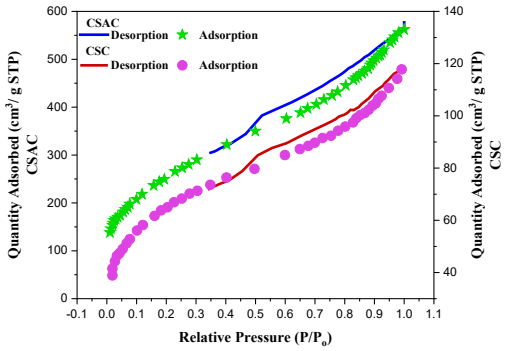

Figure 4. (a) CSC and (b) CSAC samples for N2 Adsorption-desorption isotherm.

One possible explanation is that the so-called tensile strength effect is enhanced in CSAC due to the inclusion of particle reinforcement. Given this, it's reasonable to say that CSAC has better mechanical properties than CSC [25], [26]. Comparing the textural features of carbonaceous materials, Table 1 shows that CSAC has much better results than CSC in terms of specific surface area and pore size. Carbon activation improves the textural properties of CSAC relative to CSC, since it possesses substantially greater micropore size, BET surface area, DT micropore area, and BJH volume of pores. These characteristics are comparable to those of other carbonaceous, according to the literature. Table 1 Characterization of the textural properties of carbon CSAC and BA samples via Nitrogen gas desorption - adsorption.

Factors	**Activated carbon**	**Coconut shell charcoal**
Size of micropore (nm)	1.42± 0.05	1.54± 0.04
Barrett-Joiner-Halendapore volume	0.96± 0.02	0.23± 0.05
Brumaire-Emmett-Teller surface area (m^2/g)	1161± 130	195± 27
Surface area of DA	0.52± 0.02	0.1 ± 0.05

3.4. Investigations electrochemical and electrical of the LSCF+CSAC electrode

In order to comprehend the charge diffusion of LSCF and LSCF+CSAC, the procedures outlined in session 2.7 were followed to conduct ac impedance spectroscopy measurements. Figure 5displays the frequency-specific capacitance (Cs) relationship for LSCF and LSCF+CSAC materials with an ac amplitude of 10 mV, both as-prepared and after mixing. Across the whole frequency range, LSCF+CSAC displays Cs values higher than LSCF. When the electric signal is given at lower frequencies (longer relaxation durations), it can penetrate the carbon pores more deeply. Around 263 F/g and 586 F/g, respectively, were found to be the maximal Cs of LSCF and LSCF+CSAC at 1 Hz. Comparing LSCF's Cs value to that of lanthanum perovskites yields comparable results [27], [28]. In fact, CSAC's textural and morphological features are responsible

for the increased Cs seen in LSCF+CSAC instead. A particular capacitance value between 100 and 370 F/g is possible for activated carbons [29]. It is possible that the higher Cs that were observed were caused by the combination of LSCF and CSAC.

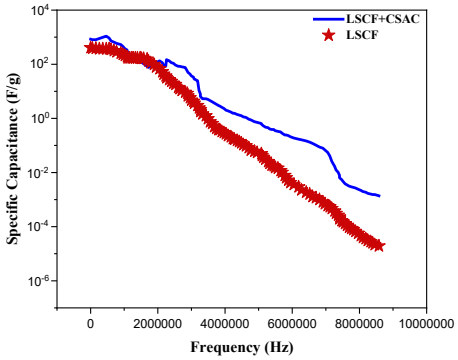

Figure 5. Current amplitude of 10 mV as a function of specific capacitance (Cs) for LSCF and LSCF+CSAC.

The real (Z′) and imaginary (Z″) component impedances of LSCF and LSCF+CSAC are displayed in the Nyquist plots in Figure 6. Along the Z′ axis, both electrodes showed low resistance semicircles. Regardless of the fact that LSCF+CSAC exhibited a greater resistance (~ 15.2Ω) compared to LSCF (~ 0.31 Ω), the more symmetrical appearance of its semicircle suggests that LSCF+CSAC maintains a consistent charge transfer from the bulk to the current collector contact. There is a connection between this quality and the improved capacitance and conductivity of LSCF made possible by CSAC's larger surface area and more porous structure. To improve the performance of the supercapacitor, it is recommended to use CSAC with LSCF as the electrode.

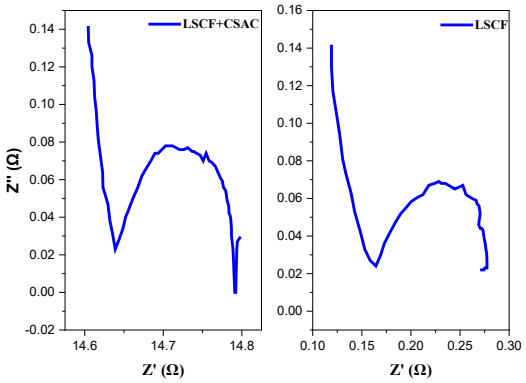

S

Figure 6. At 10 mV, a Nyquist plot was generated for the LSCF and LSCF+CSAC electrodes across a frequency range of 1 Hz to 1 MHz.

To study the electrochemical performance of the as-prepared LSCF and LSCF+CSAC, we used three electrode setup with relatively derated voltages to perform CV and GCD measurements. At scan rates of 20, 40, 60, and 100 mV/s, Fig. 7 shows the CVs of LSCF and LSCF+CSAC electrodes with potential window ranging from -0.7 to 0.7 V. Several characteristics of the CV indicate that the electrode's reaction is quasi-reversible. One thing that stands out is that the CVs aren't perfectly symmetrical for either material. Compared to reduction (negative) current peaks, oxidation (positive) ones have a better potential. The characteristic pseudocapacitive behavior observed during the transition from Mn's 3+ to 4+ states during the faradaic redox reaction is indicated by these peaks[30], [31]. Still, the CV curves of LSCF+CSAC are more deformed and rectangular, thus it stands out more.

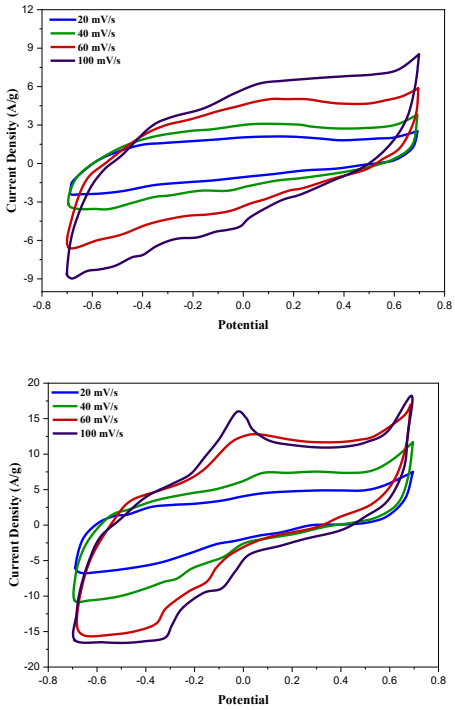

Figure 7. CV generated at various scanning rates in a 0.1 M KOH solution using LSCF and LSCF+CSAC electrodes.

The GCD profiles for LSCF and LSCF+CSAC, both operating at a constant current of 5 A/g, are shown in the insets of Figure 7. The samples were constant during the 100 cycles, which lasted about 24 seconds apiece, according to the cycling test. So, it seems like the electrode materials don't get any older by continually cycling. In order to increase the capacitors' service life, authors[32], [33] suggested doing cycle test using derated voltages. Activated carbon in inorganic electrolytes is usually used for cyclic investigations at a voltage range of 3.5-4.0 V, while metal oxides in aqueous electrolytes are normally operated at a nominal voltage range of 1.5-2.2 V. Continuous load or float testing is an alternative to cycle testing for EDLC materials. In order to quantify the capacitance over time, this test requires keeping electrode cell at nominal voltage. On the other hand, electrode materials that are held at a voltage that is either significantly higher than or very near to their nominal value for long time can experience leakage current, quick material deterioration and system instability. It is recommended to operate laboratory-scale cells with potential windows lower than the nominal voltage to prevent material stress and aging.
According to the sources, Cs is calculated from GCD and CV curves using Eqs. (3) and (4).

$$C_s = \frac{I\Delta t}{m\Delta V} \quad (3)$$

$$C_s = \frac{\int I_{(V)} dV}{m \cdot v \cdot \Delta V} \quad (4)$$

Eq. (3) reveals that LSCF+CSAC exhibited higher specific capacitances compared to LSCF during the cycling test. The capacitance of LSCF remains relatively stable at around 157 to 160 F/g, but the capacitance of LSCF+CSAC increases significantly from around 317 to 378 F/g before gradually decreasing to approximately 313 F/g as the cycles continue. Electrochemical activation may allow the ions and electrons to transfer quickly, which in turn causes a gradual accumulation of charges in the pores of CSAC, which could explain the behavior. Reduced electrochemical performance is caused by a slowdown in charge transmission, which may be due to impurities on the surface of the pores or buildup within them. Despite this, retention rate is about 98% throughout cycling test, and the capacitance decreases very little. LSCF+CSAC demonstrated superior Cs and improved capacity retention in comparison to LSCF. The enhanced durability of the composite LSCF+CSAC electrode is due to the quick electron transport on the carbon porous surface. This quality of LSCF+CSAC can be seen as advantageous for devices needing extended lifespan cycles and rate efficiency.

With the exception of a decrease in Cs values from 20 mV/s to 100 mV/s, the results of CV measurements and Equation (4) reveal that Cs values are similar to GCD values. For LSCF, the results varied between 375 and 142 F/g, while for LSCF+CSAC, the range was 823 to 261 F/g. In the electrochemical redox process, a scan rate of 60 mV/s or higher causes the positive ions in the electrolyte within the electrode to either be depleted or saturated. This reduces capacitance since only the outside surface is available for charge storage. Capacitance increases when scan speeds are less than or equal to 20 mV/s because more electrolyte negative ions can reach the electroactive sites. The two-electrode configuration allows capacitances to be saturated more quickly than the three-electrode design. Consequently, we observed that the Cs values predicted by GCD and CV and those achieved by ac impedance are equivalent in magnitude but not identical. Therefore, when the electrode thickness grows, the Cs values decrease quickly, which complicates the determination of individual energy values and accurate assessment of specific capacitance contributions [34], [35]. This means that electrochemical methods of measuring Cs are more accurate. An exceptionally high specific capacitance of 811 F/g was observed at a scan rate of 20 mV/s for LSCF+CSAC. The provided electrochemical data suggests that LSCF+CSAC could be a promising supercapacitor electrode material.

3.5 Ferroelectric characteristics of perovskites BST and ST

The ferroelectric characteristics of BST and ST were examined at room temperature using hysteresis loops as seen in Figure 8. Hysteresis loops were seen in both materials, and they were both saturated. Having said that, BST has a higher ferroelectricity than ST. At an electric field of 30 kV/cm, the maximum polarization for BST was approximately 7 μC/cm², while for ST it was around 4 μC/cm². This characteristic allows them to excel in storing electric energy.

It is appealing to use these ferroelectric materials in supercapacitors because of their crucial property, which has prospective applications. The energy density of BST and ST is shown in the inset of Figure 8. The stored energy density for BST was approximately 49 mJ/cm^3 and for ST it was around 41 mJ/cm^3, as determined by integrating the P-E curves.

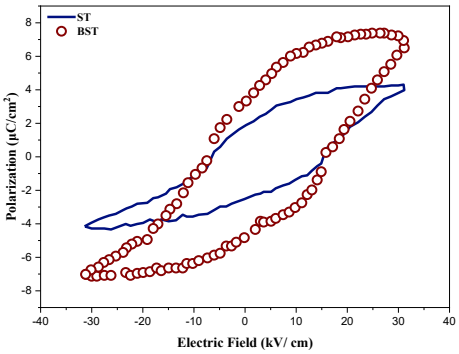

Figure 8. Polarization (P)-electric field (E) hysteresis loops are observed in perovskite ferroelectric materials of the ST and BST varieties at room temperature.

Other ferroelectric ceramics and composites, like ST/PVDF and Ba1-xSrxTi1-yZryO3, show similar polarization patterns. In addition to their high energy storage density and favorable ferroelectric properties, the crystal structure, chemical stability, and structural compatibility of BST and ST render them optimal materials for enhancing the stored energy in supercapacitors.

3.6. Assembled coin cell supercapacitor (CCS) device performance

Table 2 shows the various configurations of four-coin cell supercapacitors (CCSs) that we constructed to investigate the compatibility and quality of our synthetic materials. Using the electrochemical characterization discussed in sessions 2.11–2.13, we examined the SCs' performance using a two-electrode capacitor system.

Each CCS configuration's charge storage capability was assessed using room temperature electrochemical tests. Figure 9 shows that all of the devices had minimal contact resistance and excellent capacitive performance, with rectangular CVs observed across a potential range of 0-0.4 V and a range of scan rates (10-120 mV/s). The oxygen evolution reaction in the electrolyte might cause an excessive current density and leakage current. To achieve repetitive cycling and suppress this reaction, a potential window of 0-0.4 V was chosen. SC's excellent cyclability is demonstrated by its constant charge and discharge; across the entire voltage range, there is no faradic peak that does not result from a reduction-oxidation process. The slightly slanted rectangular shapes of the CCS devices indicate that the electrode materials transferred the ions efficiently. It appears that the electrochemical processes in CCS devices are propelled by ionic migration as opposed to diffusion, as the current at the reversal and start potentials exhibits a nearly linear relationship with the scan rate. In contrast to the other SC designs, the CVs of CCS #1 demonstrated better reversibility and charging current over extremely short curves without distortion at any scan rate, as highlighted in the text. The enhanced charge transit among electrodes and device's high-rate capability are directly related to this enhancement.

Table 2. The configuration of coin cell supercapacitors (CCSs).

Coin Cell Supercapacitor	Composition
CCS #1	Cu/LSCF+CSAC/BST/cellulose/BST/LSCF+CSAC/Al
CCS #2	Cu/LSCF+CSAC/BST/cotton/BST/LSCF+CSAC/Al
CCS #3	Cu/LSCF+CSAC/ST/cellulose/ST/LSCF+CSAC/Al
CCS #4	Cu/LSCF+CSAC/ST/cotton/ST/LSCF+CSAC/Al

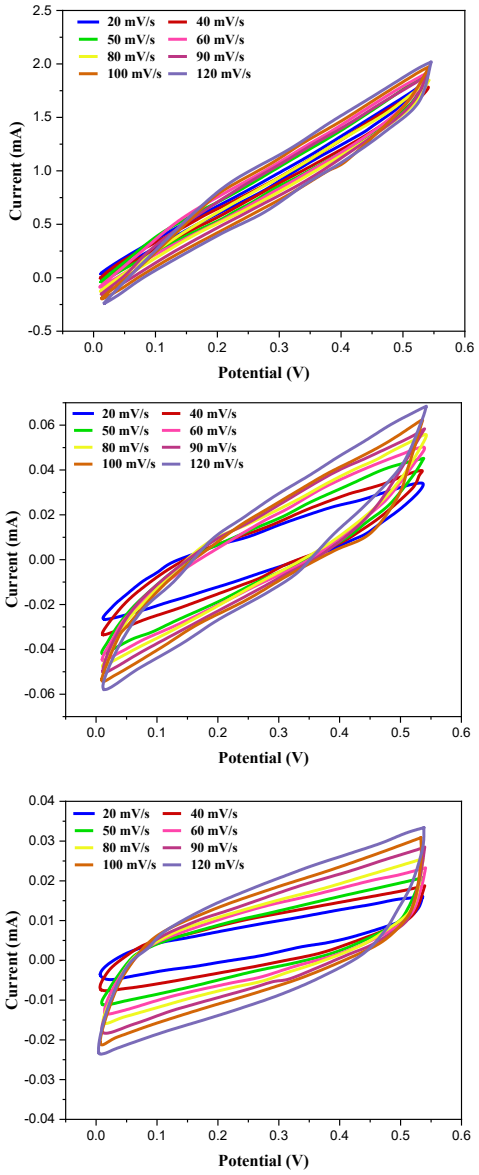

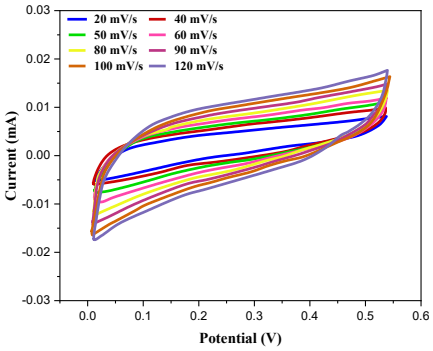

Figure 9. CCS devices captured cyclic voltammograms at various scan rates.

However, it is clear that separator materials affect CV form. Devices based on BST and ST that use cellulose exhibit enhanced performance. The separator's electrical insulating properties are essential in SC devices for preventing short circuits and facilitating electrolyte migration toward the electrode surface when using electrodes with opposite polarization. As an eco-friendly substitute for SC devices, cellulose offers a number of benefits, including surface porosity, roughness, large surface area, and electrolyte absorption. Whereas CCS #1 performed admirably, CCS #2, which relies on cotton fabric lint separators, was far less effective. CCS devices utilizing cellulose demonstrated uniformly higher currents at 0.5V for scan rates when compared to those utilizing cotton fabric fibers. The CCS devices based on BST (SC #1 and 2) exhibit a more pronounced differentiation in this regard when contrasted with those based on ST (SC #3 and 4). The currents determined for specific SCs at 0.5V and 125mV/s as follows: CCS #1 delivered 1.74 mA, CCS #2 delivered 0.057 mA, CCS #3 delivered 0.0283 mA, and CCS #4 delivered 0.0138 mA. According to these results, BST-cellulose-based CCS devices enable charge spread with electrolyte towards LSCF+CSAC electrodes at a faster rate.

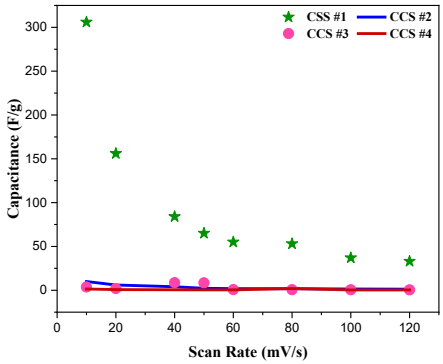

Figure 10. Capacitance specific to CCS devices as a function of scan rate.

Observe the variation in the capacitance (Cs) values of the CCS devices with different scanning rates as illustrated in Figure 10, which are calculated from the cyclic voltammetry (CV) curves using Equation (4). It was observed that as the potential scan rate increases, the Cs values decrease.

Each of the four CCSs had a Cs value of 305 F/g, 10 F/g, 3.7 F/g, and 1.4 F/g at the lowest scan rate. With significantly greater Cs values, CCS #1 stands out from the other CCS devices. In most cases, the capacitive properties of CCS devices based on cellulose showed better performance than those of the lint separator made of cotton fiber. The dependence of the effective conductivity (σ) and density (ρ) of separator materials on the voltage range V may be associated with the electrolyte depletion effect. Because of their higher effective conductivity, cellulose separators may improve Cs while having less of an effect on the starving molar conductivity of ions. The maximal capacitance is highly dependent on the separator material utilized for BST-based systems operating at low scan speeds (v ≤ 20 mV/s). The maximum capacitance in ST-based devices, on the other hand, is only weakly dependent on the separator material. This behavior may be attributed to the high specific capacitance of the BST/cellulose device, which is produced by combining a mobile space charge layer with a substantial effective electrode area. Moreover, considering the similar electrical resistivities of BST and ST (approximately 1 × 109 Ω.cm for ST) and the lower density of BST compared to ST (approximately 4 × 109 Ω.cm for BST), it is logical to hypothesize that the ions of BST will encounter fewer obstacles in their pursuit of greater mobility within the electrolyte with respect to the LSCF+CSAC.

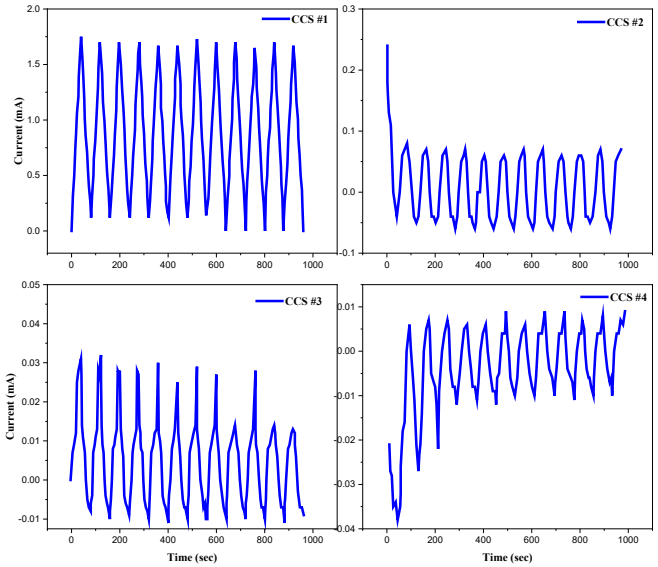

Figure 11. CCS device galvanostatic charge/discharge (GDC) curves.

Figure 11 illustrates the galvanostatic discharge - charge curvatures for CCS devices. All the devices are triangular curves, with CCS #1 showcasing symmetrical curvature indicative of nearly ideal capacitive behavior. Devices equipped with cotton fabric lint separators showed a more pronounced decline in the discharge phase compared to other CCS devices. CCS devices using cellulose exhibited a higher peak current than those using cotton fabric dust, yet had similar charge-discharge durations. The maximum current for ST based device was lower than BSTbased device, attributed to diffusion in the electrolyte and slower ion movement. Conversely, CCS devices #3 (96%), #2 (97%), and #1 (98%) maintained high retention rates, while CCS #4 exhibited the lowest retention rate (40%) after 12 successive charge-discharge cycles.

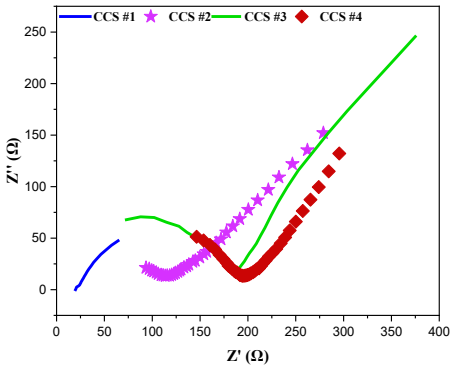

Figure 12. The modeling and Nyquist plots of CCS device electrochemical impedance.

The electrochemical impedance properties of the CCS devices under examination are shown in Figure 12 by use of Nyquist's diagrams. Every single SC clearly displayed the electrochemical impedance of an EDLC, which is represented as a semicircular curve at high frequencies and a sharply rising straight line at low frequencies. The positive capacitive behavior of the SCs is indicated by this. For CCS devices using BST/cellulose (CCS #1) and BST/cotton (CCS #2), the equivalent series resistance or electrolyte is around 20 Ω and 50 γ, respectively, according to the depressed semicircles and x-axis intercept. However, for ST/cellulose (CCS #3) and ST/cotton (CCS #4), the predicted Rs values are approximately 3.2 Ω and 25 Ωindicating that internal resistance of electrode and the electrolyte conductivities are sufficient. All CCSs use different electroactive materials and separators, which have a major impact on the Rs. Assuming the composition of electrode, current collectors, and electrolyte concentration are held constant, a sole factor contributing to variations in Rs values is the differences in the properties of the separator material and electroactive materials.

It is the electrolyte's wettability on the separator's surface that mostly causes the Rs values to vary. The idea that the electrochemical characteristics are improved and the Rs is decreased due to the presence of ionic mobility in the electrolyte containing cellulose may be supported by this factor. In Figure 12, separate red lines depict the fitting procedure to the experimental data. Figure 13 shows the modeling to an integral equivalent circuit. The corresponding series resistor for the whole CCS device is Rs, while the pseudo-capacitance is CF. To mimic the double-layer capacitance and faradaic impedance of the electrode/electrolyte, CPEdl—a configuration of constant phase element and RF was used. The electrodes were represented by a constant phase element termed CPEele and a parallel configuration of Rele.

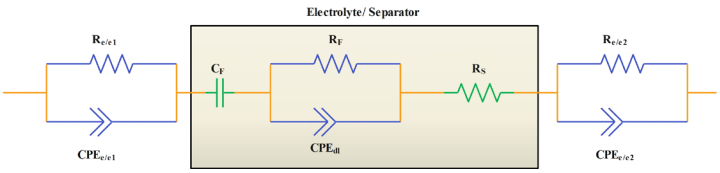

Figure 13. A model of the integral equivalent circuit that depicts the dynamic electrical behavior of CCS devices.

To validate and build models of the CCS devices' dynamic electrical properties, the researchers used electrochemical analyzers. Given the dispersed impedance response observed in our heterostructure supercapacitor designs, it is possible to incorporate a distributing factor (n) into the model. Constant phase elements (CPEs) are therefore incorporated so that the SC conduction mechanisms can be comprehended more realistically. A well-known way to describe the impedance of CPE is:

$$Z_{CPE} = \frac{1}{A(j\omega)^n} \quad (5)$$

The selection of CPEs is based on their ability to depict the two-layer interface and the rough, porous surface of the electrode. Here are the real and imaginary components of the impedance, according to the method for rough surfaces:

$$Z'(\omega) = \frac{R_1}{1+(A_1 \cdot R_1 \cdot \omega^{n_1})^2} + \frac{R_2}{1+(A_2 \cdot R_2 \cdot \omega^{n_2})^2} + \frac{R_3}{1+(A_3 \cdot R_3 \cdot \omega^{n_3})^2} + R_4 \quad (6)$$

$$Z'(\omega) = \frac{A_1 R_1^2 \omega^{n_1}}{1+(A_1 \cdot R_1 \cdot \omega^{n_1})^2} + \frac{A_2 R_2^2 \omega^{n_2}}{1+(A_2 \cdot R_2 \cdot \omega^{n_2})^2} + \frac{A_3 R_3^2 \omega^{n_3}}{1+(A_3 \cdot R_3 \cdot \omega^{n_3})^2} + \frac{1}{\omega C} \quad (7)$$

Where:
$R_1 = R_{ele1}$, $R_2 = R_{ele2}$, $R_3 = R_F$ and $R_4 = Rs$
$A_1 = CPE_{ele1}$, $A_2 = CPE_{ele2}$, $A_3 = CPE_{dl}$ and $C = C_F$

Finally, a yellow LED set up was fixed (with a minimum working potential of 1.75 V) by connecting two identically built CCS #1 devices in series. This allowed us to confirm the device's applicability for practical applications even further. While keeping track of how long the LED remained on, the setup was powered up to 5 V and linked to the light source. Good power and energy density were on display as the LED steadily dimmed after emitting a brilliant light for almost 1 minute. This continued for about 2.5 more minutes. Table 3 displays the power densities and energy densities of CCS devices derived from experimental data and applied to Eqs. (1) and (2). Based on these measures, CCS #1 performs exceptionally well in comparison to current energy storage systems. Its power density is 600 W/kg and energy density is 6.7 Wh/kg, which are significantly higher. Power densities of supercapacitors for energy storage applications range from 10-105 W/kg, while energy densities range from 1 to 9 Wh/kg, as per Ragone's relationship. Because of this, the CCS #1 is an excellent choice for the task.

Table 3. The power density and maximum energy density of CCS devices**.**

Configuration	Maximum density for Power	Maximumdensity for Energy
CCS #1	600	6.7
CCS #2	12.3	0.14
CCS #3	5.4	0.06
CCS #4	1.8	0.02

4. CONCLUSION

With the utilization of the spray pyrolysis method, we have effectively manufactured and incorporated a variety of perovskite materials (LSCF, BST, and ST) and CSAC into electrochemical supercapacitor devices. The final device configurations were accomplished by employing cellulose and cotton lint immersed in PVP/H_3PO_4 as the separator and electrolyte, respectively. All sorts of supercapacitors in coin cell shapesare tested for chemical resistance, structural soundness, compatibility, and overall quality. Devices of the coin cell type that were self-assembled were tested using electrochemical characterization techniques such as electrochemical impedance spectroscopy, cyclic voltammetry, and galvanostatic charge/discharge. The experimental data was represented and modeled using equivalent circuits to improve understanding of the charge-discharge mechanisms and electrochemical process. Among all tested supercapacitor configurations, the BST/cellulose (CCS #1) setup exhibited superior performance across key metrics including specific capacitance, power density, energy density, and retention rate, positioning it as an optimal choice for future energy storage applications.

In conclusion, the practical applicability of the LED is demonstrated by how long it remains illuminated when powered on. For increased longevity and efficiency, the supercapacitors fabricated using our method might necessitate additional monitoring and analysis of their deterioration and aging. The efficacy assessment examining the utilization of perovskite materials in conjunction with CSAC yielded encouraging outcomes and may expedite the development of electrochemical hybrid supercapacitors that are economical, lightweight, flexible, and wearable for energy storage purposes.

REFERENCES

[1] F. Hadji, M. Omari, M. Mebarki, N. Gabouze, and A. Layadi, "Zinc doping effect on the structural and electrochemical properties of LaCoO3 perovskite as a material for hybrid supercapacitor electrodes," *J Alloys Compd*, vol. 942, 2023. DOI:10.1016/j.jallcom.2023.169047

[2] Guan Fu Liu, Pian Pian Ma, Yin Qiao, Ren Hao Xu, De Meng Huang, Rui Yang Hu, Li Yuan Liu a, Guo Hua Jiang, Muslum Demir, 2022 "Perovskite SrCo1-xTixO3-δ as anion-intercalated electrode materials for supercapacitors," *J Energy Storage*, vol. 52. DOI:10.1016/j.est.2022.104942

[3] T. A. Amibo, S. M. Beyan, M. Mustefa, V. P. Sundramurthy, and A. B. Bayu, "Development of

Nanocomposite based Antimicrobial Cotton Fabrics Impregnated by Nano SiO2 Loaded AgNPs Derived from Eragrostis Teff straw," *Materials Research Innovations*, vol. 26, no. 7, pp. 405–414, 2022. DOI:10.1080/14328917.2021.2022372

[4] R. Mondal, N. K. Mishra, T. Maiyalagan, A. Gupta, and P. Singh, "La1-xK xFeO3-δ: An Anion Intercalative Pseudocapacitive Electrode for Supercapacitor Application," *ACS Omega*, vol. 6, no. 45, pp. 30488–30498, 2021. DOI:10.1021/acsomega.1c03902

[5] Shyamli Ashok C, Ashalatha Vazhayil, R. Vinaykumar, Jasmine Thomas, A. Anto Jeffery, Imran Hasan, Nygil Thomas, Akhilesh Kumar Yadav, Young-Ho Ahn, 2024, "The effect of B – site cation on the super capacitive properties of LaBO3 (B = Cr, Mn, Fe and Co) porous perovskites," *J Energy Storage*, vol. 86. DOI:10.1016/j.est.2024.111145

[6] P. Muruganandhan, S. Jothilakshmi, R. Vivek, S. Nanthakumar, S. Sakthi, S. Mayakannan and R. Girimurugan, 2023, "Investigation on silane modification and interfacial UV aging of flax fibre reinforced with polystyrene composite," *Mater Today Proc*. DOI:10.1016/j.matpr.2023.03.272

[7] Sarmad Iqbal, Amr Hussein Mady, Young-Il Kim, Umer Javed, P. Muhammed Shafi, Van Quang Nguyen, Iftikhar Hussain, Dirk Tuma and Jae-Jin Shim, 2021, "Self-templated hollow nanospheres of B-site engineered non-stoichiometric perovskite for supercapacitive energy storage via anion-intercalation mechanism," *J Colloid Interface Sci*, vol. 600, pp. 729–739. DOI:10.1016/j.jcis.2021.03.147

[8] Sathish, T., Chandramohan, D., Vijayan, V., Sebastian, P.J. (2019). Investigation on microstructural and mechanical properties of Cu reinforced with Sic composites prepared by microwave sintering process. Journal of New Materials for Electrochemical Systems, Vol. 22, No. 1, pp. 5-9. DOI:10.14447/jnmes.v22i1.a02

[9] S. Venkatesa Prabhu, G. Ramesh, A. T. Adugna, S. M. Beyan, and K. Gizachew Assefa, "Kinetics of iron bioleaching using isolated leptospirillum ferriphilum: Effect of temperature," *International Journal of Innovative Technology and Exploring Engineering*, vol. 8, no. 12, pp. 76–81, 2019. DOI:10.35940/ijitee.L3210.1081219

[10] Fatma Mohamed Mahgoub1,2*, S. M. Al-Rashdi3, 2016 "Investigate the Corrosion Inhibition of Mild Steel in Sulfuric Acid Solution by Thiosemicarbazide," Journal of Physical Chemistry, vol. 6, pp. 54-66. DOI:10.4236/ ojpc.2016.63006

[11] Sankar, L.P., Kamalakannan, R., Aruna, G., Meera, M.R., Vijayan, V., Sivananthan, S. (2020). Mechanical behavior and microstructure evolution of Al-5%Cu/TiC metal matrix composite. Journal of New Materials for Electrochemical Systems, Vol. 23, No. 4, pp. 252-255. DOI:10.14447/jnmes.v23i4.a05

[12] Ying, Danfeng and Ding, Rui and Huang, Yongfa and Shi, Wei and Xu, Qilei and Tan, Caini and Sun, Xiujuan and Gao, Ping and Liu, Enhui, 2019, "Conversion pseudocapacitance-contributing and robust hetero-nanostructural perovskite KCo0.54Mn0.46F3 nanocrystals anchored on graphene nanosheet anodes for advanced lithium-ion capacitors, batteries and their hybrids," *J Mater Chem A Mater*, vol. 7, no. 31, pp. 18257–18266. DOI:10.1039/C9TA06438A

[13] Loganathan, M., Dinesh, S., Vijayan, V., Karuppusamy, T., Rajkumar, S. (2020). Investigation of mechanical behaviour on composites of Al6063 alloy with silicon, graphite and fly ash. Journal of New Materials for Electrochemical Systems, Vol. 23, No. 1, pp. 36-39. DOI:10.14447/jnmes.v23i1.a07

[14] Venkatramanan Varadharajan, Dilip Saravanan Senthilkumar, Kathiresan Senthilkumar, Venkatesa Prabhu Sundramurthy, Rahul Manikandan, Hariprasath Senthilarasan, Harish Ganesan, Indiravadanan Kesavamoorthy, Arulvel Ramasamy, 2022, "Process modeling and toxicological evaluation of adsorption of tetracycline onto the magnetized cotton dust biochar," *Journal of Water Process Engineering*, vol. 49. DOI:10.1016/j.jwpe.2022.103046

[15] B. Tessema, G. Gonfa, S. Mekuria Hailegiorgis, and S. Venkatesa Prabhu, 2023 "An Overview of Current and Prognostic Trends on Synthesis, Characterization, and Applications of Biobased Silica," *Advances in Materials Science and Engineering*, vol. 2023. DOI:10.1155/2023/4865273

[16] Hongwei Tian, Xueqin Lang, Haoshan Nan, Ping An, Wei Zhang, Xiaoying Hu and Jinshui Zhang, 2019 "Nanosheet-assembled LaMnO3@NiCo2O4 nanoarchitecture growth on Ni foam for high power density supercapacitors," *Electrochim Acta*, vol. 318, pp. 651–659. DOI:10.1016/j.electacta.2019.06.133

[17] A. Afif, S. M. Rahman, A. Tasfiah Azad, J. Zaini, M. A. Islam, and A. K. Azad, 2019, "Advanced materials and technologies for hybrid supercapacitors for energy storage – A review," *J Energy Storage*, vol. 25. DOI:10.1016/j.est.2019.100852

[18] R. Girimurugan, G. B. Loganathan, G. Sivaraman, C. Shilaja, and S. Mayakannan, 2022, "Compressive Behavior of Tamarind Shell Powder and Fine Granite Particles Reinforced Epoxy Matrix Based Hybrid Bio-Composites," in *ECS Transactions*, Institute of Physics, pp. 7111–7118. DOI:10.1149/10701.7111ecst

[19] R. Jayaraman, R. Girimurugan, V. Suresh, C. Shilaja, and S. Mayakannan, 2022, "Improvement on Tensile Properties of Epoxy Resin Matrix Sugarcane Fiber and Tamarind Seed Powder Reinforced Hybrid Bio-Composites," in *ECS Transactions*, Institute of Physics,22, pp. 7265–7272. DOI:10.1149/10701.7265ecst

[20] S. Thangaraj, G. M. Pradeep, M. S. Heaven Dani, S. Mayakannan, and A. Benham, 2022, "Experimental investigations on tensile and compressive properties of nano alumina and arecanut shell powder reinforced polypropylene hybrid composites," in *Materials Today: Proceedings*, Elsevier Ltd, pp. 2243–2248. DOI:10.1016/j.matpr.2022.08.442

[21] T. Bothiraj, K. Boopathi, K. Kalaiselvan, A. Benham, and S. Mayakannan, 2022, "Experimental investigations on mechanical and wear behavior of waste marble dust and coconut fiber reinforced hybrid bio composites," in *Materials Today: Proceedings*, Elsevier Ltd, pp. 2239–2242.

[22] S. Mayakannan, R. Rathinam, Rajasekaran Saminathan, R. Deepalakshmi, Mahesh Gopal, J. Justin Maria Hillary, S. Nanthakumar, V. Y. Ganvir, Pallavi Singh, 2022

"Analysis of Spectroscopic, Morphological Characterization and Interaction of Dye Molecules for the Surface Modification of TiB2 Nanoparticles", Journal of Nanomaterials, vol. 2022, Article ID 1033216, 9 pages. DOI:10.1155/2022/1033216

[23] N. M. Keppetipola, C. Olivier, T. Toupance, and L. Cojocaru, "Biomass-derived carbon electrodes for supercapacitors and hybrid solar cells: Towards sustainable photo-supercapacitors," *Sustain Energy Fuels*, vol. 5, no. 19, pp. 4784–4806, 2021. DOI: 10.1039/D1SE00954K

[24] A. Roy, F. E. Cancino-Gordillo, S. Saha, U. Pal, and S. Das, "Performance of asymmetric supercapacitor fabricated with perovskite-type Sr2+-incorporated LaMnO3 (La0.7Sr0.3MnO3) nanostructures in neutral 1M Na2SO4 aqueous electrolyte," *Int J Energy Res*, vol. 45, no. 9, pp. 14021–14033, 2021. DOI:10.1002/er.6727

[25] Xueqin Lang, Haifeng Zhang, Xin Xue, Chuanlu Li, Xucong Sun, Zitang Liu, Haoshan Nan, Xiaoying Hu and Hongwei Tian, 2018 "Rational design of La0.85Sr0.15MnO3@NiCo2O4 Core–Shell architecture supported on Ni foam for high performance supercapacitors," *J Power Sources*, vol. 402, pp. 213–220. DOI:10.1016/j.jpowsour.2018.09.040

[26] N. Lei, P. Ma, B. Yu, S. Li, J. Dai, and G. Jiang, "Anion-intercalated supercapacitor electrode based on perovskite-type SrB0.875Nb0.125O3 (B = Mn, Co)," *Chemical Engineering Journal*, vol. 421, 2021. DOI:10.1016/j.cej.2020.127790

[27] Z. Jia *et al.*, "Unraveling the Charge Storage and Activity-Enhancing Mechanisms of Zn-Doping Perovskite Fluorides and Engineering the Electrodes and Electrolytes for Wide-Temperature Aqueous Supercabatteries," *Adv Funct Mater*, vol. 32, no. 1, 2022. DOI:10.1002/adfm.202107674

[28] Zeyu Hao, Zeshuo Meng, Xinyue Li, Xucong Sun, Jian Xu, Haoshan Nan, Wei Shi, Gongjin Qi, Xiaoying Hu, Hongwei Tian, 2022"Two-step fabrication of lanthanum nickelate and nickel oxide core-shell dandelion-like materials for high-performance supercapacitors," *J Colloid Interface Sci*, vol. 617, pp. 430–441. DOI:10.1016/j.jcis.2022.03.001

[29] P. Lannelongue, S. Le Vot, O. Fontaine, T. Brousse, and F. Favier, 2019, "Electrochemical study of asymmetric aqueous supercapacitors based on high density oxides: C/Ba0.5Sr0.5Co0.8Fe0.2O3-δ and FeWO4/Ba0.5Sr0.5Co0.8Fe0.2O3-δ," *Electrochim Acta*, vol. 326. DOI:10.1016/j.electacta.2019.134886

[30] K.-P. Cheng, R.-J. Gu, and L.-X. Wen, 2020, "Application of a clustered countercurrent-flow micro-channel reactor in the preparation of KMnF3 perovskite for asymmetric supercapacitors," *RSC Adv*, vol. 10, no. 20, pp. 11681–11693. DOI:10.1039/D0RA01411G

[31] Y. Cao, B. Lin, Y. Sun, H. Yang, and X. Zhang, 2015, "Symmetric/Asymmetric Supercapacitor Based on the Perovskite-type Lanthanum Cobaltate Nanofibers with Sr-substitution," *Electrochim Acta*, vol. 178, pp. 398–406. DOI:10.1016/j.electacta.2015.08.033

[32] Zeshuo Meng, Jian Xu, Peixin Yu, Xiaoying Hu, Yixian Wu, Qi Zhang, Yaxin Li, Liang Qiao, Yi Zeng, Hongwei Tian,, 2020, "Double perovskite La2CoMnO6 hollow spheres prepared by template impregnation for high-performance supercapacitors," *Chemical Engineering Journal*, vol. 400. DOI:10.1016/j.cej.2020.125966

[33] B. Zhang, P. Liu, Z. Li, and X. Song, 2021 "Synthesis of two-dimensional sr-doped lanio 3 nanosheets with improved electrochemical performance for energy storage," *Nanomaterials*, vol. 11, no. 1, pp. 1–13. DOI:10.3390/nano11010155

[34] I. Ajin, R. Balamurugan, and A. Chandra Bose, 2023. "Tailoring the Perovskite Structure to Acquire an Inorganic La2NiCrO6 Double Perovskite as an Efficient Energy Storage Application by Varying Molar Concentrations of Citric Acid," *ACS Appl Energy Mater*, vol. 6, no. 18, pp. 9764–9777. DOI:10.1021/acsaem.3c01908

[35] A. R. Tobi and J. O. Dennis, 2021, "Activated carbon from composite of palm bio-waste as electrode material for solid-state electric double layer capacitor," *J Energy* Storage, vol. 42. DOI:10.1016/j.est.2021.103087

[36] S.Dinesh, A.Godwin Antony, S.Karuppusamy, V.Vijayan and B.Suresh Kumar, 2016. Experimental investigation and optimization of machining parameters in CNC turning operation of duplex stainless steel. Asian Journal of Research in Social Sciences and Humanities 6,pp. 179-195. DOI:10.5958/2249-7315.2016.01006.6

[37] S.Dinesh, A.Godwin Antony, K.Rajaguru and V.Vijayan. 2016. Investigation and Prediction of material removal rate and surface roughness in CNC turning of EN24 alloy steel, Asian Journal of Research in Social Sciences and Humanities , vol 6 (8) 849—863. DOI:10.5958/2249-7315.2016.00654.7

[38] T.Tamizharasan, N.Senthil Kumar, V.Selvkumar, S.Dinesh, 2019. Taguchi's Methodology of optimizing turning parameters over chip thickness ratio in machining PM AMMC, SN Appl. Sci. 1: 160., Springer Publishers. DOI:10.1007/s42452-019-0170-8